This is the accepted manuscript made available via CHORUS. The article has been published as:

Photocontrol of spin scalar chirality in centrosymmetric itinerant magnets

Atsushi Ono and Yutaka Akagi

Phys. Rev. B **108**, L100407 — Published 27 September 2023

DOI: 10.1103/PhysRevB.108.L100407

Photocontrol of spin scalar chirality in centrosymmetric itinerant magnets

Atsushi Ono[1] and Yutaka Akagi[2]

[1]*Department of Physics, Tohoku University, Sendai 980-8578, Japan*
[2]*Department of Physics, Graduate School of Science, The University of Tokyo, 7-3-1 Hongo, Tokyo 113-0033, Japan*

(Dated: August 30, 2023)

Noncoplanar magnetic structures, such as magnetic skyrmions, are characterized by the spin chirality and usually favored by antisymmetric exchange interactions in noncentrosymmetric magnets. Here, we show that a linearly polarized electric-field pulse stabilizes a nonequilibrium spin-scalar-chiral state in a centrosymmetric itinerant ferromagnet. The scalar chirality has a non-monotonic dependence on the electric-field strength, and its sign can be controlled by circular polarization. Furthermore, magnetic skyrmions are excited after the pulse decays. A photoinduced non-thermal electron distribution plays an important role for instability towards the spin-scalar-chiral state as well as the 120° Néel state, depending on the next-nearest-neighbor transfer integral. These results provide an alternative route to controlling the spin chirality by photoirradiation.

Introduction.—Swirling spin textures, e.g., magnetic bubbles, vortices, and skyrmions, have been intensively studied in condensed matter physics [1–11]. These noncoplanar spin orders are usually attributed to the competition between the ferromagnetic (FM) interaction and the antisymmetric Dzyaloshinskii–Moriya (DM) interaction, the latter of which is present in noncentrosymmetric systems. Recently, the skyrmion crystal was discovered even in centrosymmetric magnets without the DM interaction [12–15], where, e.g., the geometrical frustration, magnetic anisotropy, and Fermi-surface instability play a role in generating the spin chirality [16–24]. When electrons are subject to the emergent fields associated with the noncoplanar or noncollinear spin structure, intriguing transport [25–31] and optical [32–36] phenomena are observed, thereby attracting scientific and technological interest.

In the past decade, it has been demonstrated that optical pulses enable the ultrafast control of the spin chirality. In multiferroics, the magnetic structure can be switched by terahertz pulses or X-ray irradiation [37–41]. Also, many researchers have studied the optical creation of the skyrmions in the noncentrosymmetric magnets, where the local excitation by laser promotes the nucleation of the skyrmions [42–50]. The nonthermal control of the magnetic interactions and spin chirality via high-frequency laser, microwave, and static fields was also proposed theoretically [40, 51–68]. For example, circularly polarized light breaks the time-reversal symmetry and can be coupled to the scalar chirality [54–59]. Since linearly polarized light and a static electric field break the inversion symmetry, they can modulate or induce the DM interaction and magnetic anisotropy [66–68]. However, these studies have considered the noncentrosymmetric systems where the DM interaction is present or dynamically induced through the spin-orbit coupling, except for Refs. [64, 65] discussing spin vector chirality.

In this study, we investigate the real-time dynamics induced by an electric field in a centrosymmetric itinerant ferromagnet described by the double-exchange model on the triangular lattice. A detailed ground-state phase diagram of this model was shown in Ref. [20]; a four-sublattice spin-scalar-chiral state [see Figs. 1(a) and 1(b)] is present near 1/4 and 3/4 fillings, exhibiting the anomalous Hall effect. First, we show that a static electric field can stabilize either the spin-scalar-chiral state or the 120° Néel state on a picosecond timescale and obtain a schematic "steady-state phase diagram" shown in Fig. 1(c). A non-thermal electron distribution due to irradiation induces the instability to these nonequilibrium steady states. Then, we demonstrate that the sign of the scalar chirality can be selected by circular polarization. The steady states with scalar chirality are induced by a terahertz pulse as well. Finally, we show that metastable magnetic skyrmions emerge after the pulse irradiation.

Model and method.—We consider the FM Kondo lattice model on the triangular lattice defined by the Hamiltonian

$$\mathcal{H} = \sum_{ijs} h_{ij} c^{\dagger}_{is} c_{js} - J \sum_{iss'} c^{\dagger}_{is} \boldsymbol{\sigma}_{ss'} c_{is'} \cdot \boldsymbol{S}_i. \tag{1}$$

Here, $c^{\dagger}_{is}$ (c_{is}) denotes the creation (annihilation) operator of an itinerant electron with spin s ($= \uparrow, \downarrow$) at site i, and the vectors $\boldsymbol{\sigma}$ and $\boldsymbol{S}_i$ represent the Pauli matrix and a classical spin localized at site i with $|\boldsymbol{S}_i| = 1$, respectively. The coefficients h_{ij} and J denote the transfer integral and exchange interaction, respectively. We assume that $h_{ij} = -h_1$ for the nearest neighbor (NN), $h_{ij} = -h_2$ for the next nearest neighbor (NNN), and $h_{ij} = 0$ for the rest, and adopt a finite cluster of $N = 12 \times 12$ sites with periodic boundary conditions. The parameters are set to $J/h_1 = 8$, $h_2/h_1 = 0.2$–0.5, and $N_e/N = 1/4$ with N_e being the number of electrons (i.e., 1/8 filling) so that the ground state is a FM metallic state.

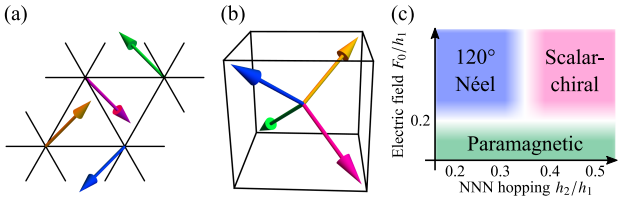


FIG. 1. (a) Snapshot of spin vectors in a four-sublattice spin-scalar-chiral state. (b) The four spin vectors point to the four vertices of a regular tetrahedron. (c) Schematic "steady-state phase diagram."

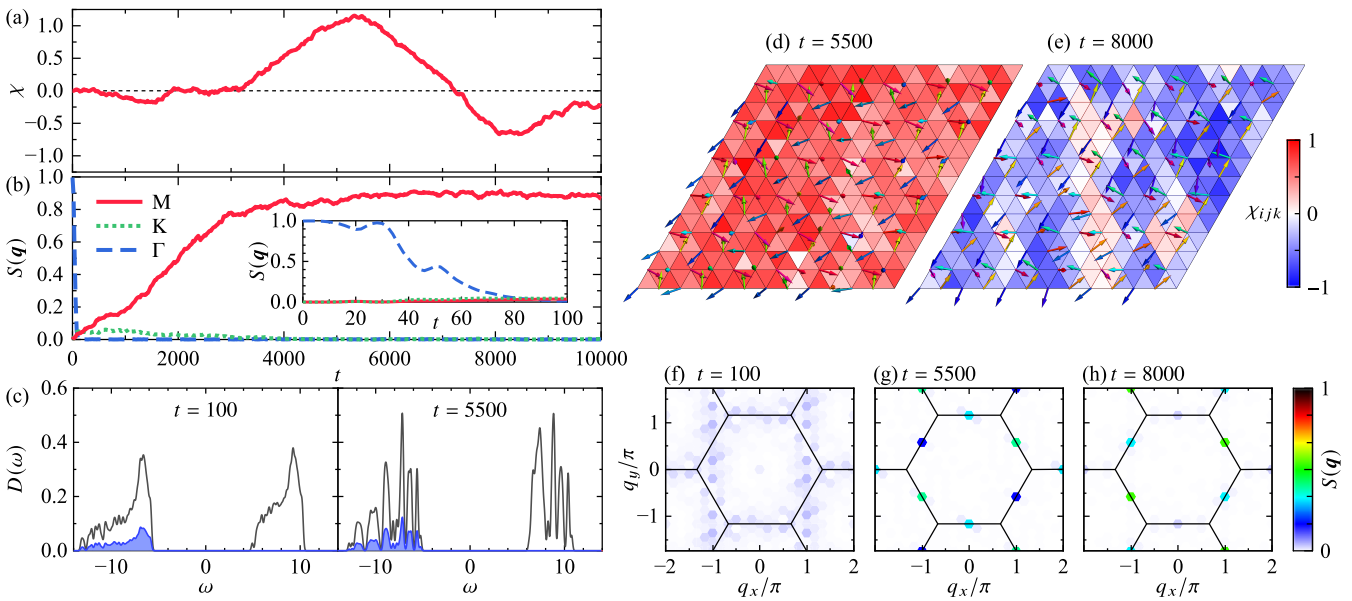


FIG. 2. (a),(b) Time profiles of (a) the spin scalar chirality and (b) the spin structure factor with a static electric field. Inset in (b) is an enlarged view. (c) Density of states $D(\omega) = \sum_\nu \delta(\omega - \varepsilon_\nu)$ (gray solid lines) and the occupation $\sum_\nu n_\nu \delta(\omega - \varepsilon_\nu)$ (blue shades). (d),(e) Snapshots of the localized spins and local spin chirality. The arrow colors indicate the in-plane angles. (f)–(h) Spin structure factor in reciprocal space. The solid lines indicate the Brillouin zone boundary. NNN transfer integral is set to $h_2 = 0.4$ in (a)–(h).

Hereafter, the elementary charge e, Dirac constant $\hbar$, lattice constant a, and NN transfer integral h_1 are set to unity; energy, time, and electric-field strength are expressed in units of h_1, $\hbar/h_1 = 0.66$ fs, and $h_1/(ea) = 20$ MV/cm for $h_1 = 1$ eV and $a = 5$ Å, respectively. An external vector potential $\boldsymbol{A}$ is incorporated via the Peierls substitution $h_{ij} \to h_{ij} e^{i\boldsymbol{A}(t)(\boldsymbol{r}_i - \boldsymbol{r}_j)}$, where t denotes time and $\boldsymbol{r}_i$ is the position of site i. The time evolution of the electrons and spins is governed by the von Neumann equation $\dot{\rho} = -i[\mathcal{H}, \rho]$ and the Landau–Lifshitz–Gilbert (LLG) equation $\dot{\boldsymbol{S}}_i = \boldsymbol{S}_i \times \boldsymbol{b}_i - \alpha \boldsymbol{S}_i \times \dot{\boldsymbol{S}}_i$, respectively [69–73]. Here, $\rho_{is,js'} = \langle c^\dagger_{js'} c_{is} \rangle$ is the one-body density matrix of the electrons, $\boldsymbol{b}_i$ represents an effective field given by $\boldsymbol{b}_i = -\partial \langle \mathcal{H} \rangle / \partial \boldsymbol{S}_i$, and α denotes the Gilbert damping constant. These equations are solved by the fourth-order Runge–Kutta method with a time step of $\delta t = 0.01$. Even though dissipation is introduced only in the LLG equation, the electrons are relaxed and scattered via the coupling term [69]. By diagonalizing the Hamiltonian at time t, we can obtain the single-particle energy level $\varepsilon_\nu(t)$ and its occupation number $n_\nu(t)$. The damping constant is set to $\alpha = 1$. We introduce a random tilt from the FM ground state up to $\delta\theta_{\max} = 0.1$ rad into $\{\boldsymbol{S}_i\}$ at $t = 0$, which mimics thermal fluctuations [69]; we need to consider the average over the initial configurations of $\{\boldsymbol{S}_i\}$ when discussing the macroscopic spin-texture dynamics.

To investigate the dynamics of the magnetic structure, we consider the spin scalar chirality $\chi = N^{-1} \sum_i (\chi_{\boldsymbol{r}_i, \boldsymbol{r}_i + \boldsymbol{a}_1, \boldsymbol{r}_i + \boldsymbol{a}_2} + \chi_{\boldsymbol{r}_i + \boldsymbol{a}_1 + \boldsymbol{a}_2, \boldsymbol{r}_i + \boldsymbol{a}_2, \boldsymbol{r}_i + \boldsymbol{a}_1})$, where $\boldsymbol{a}_1 = (1, 0)$, $\boldsymbol{a}_2 = (1/2, \sqrt{3}/2)$, and $\chi_{\boldsymbol{r}_i, \boldsymbol{r}_j, \boldsymbol{r}_k} = \chi_{ijk} = \boldsymbol{S}_i \cdot (\boldsymbol{S}_j \times \boldsymbol{S}_k)$. We also compute the spin structure factor defined by $S(\boldsymbol{q}) = N^{-2} \sum_{ij} \boldsymbol{S}_i \cdot \boldsymbol{S}_j e^{i\boldsymbol{q} \cdot (\boldsymbol{r}_i - \boldsymbol{r}_j)}$, which satisfies $S(-\boldsymbol{q}) = S(\boldsymbol{q})^* = S(\boldsymbol{q})$ and $\sum_{\boldsymbol{q}} S(\boldsymbol{q}) = 1$. Considering that $S(\boldsymbol{q})$ has a peak at the M (K) point in the spin-scalar-chiral (120° Néel) state, we define $S(\mathrm{M}) = S(\pi, -\pi/\sqrt{3}) + S(\pi, \pi/\sqrt{3}) + S(0, 2\pi/\sqrt{3})$ and $S(\mathrm{K}) = S(4\pi/3, 0) + S(2\pi/3, 2\pi/\sqrt{3})$. Note that $|\chi| = 8/(3\sqrt{3}) \approx 1.54$ and $S(\mathrm{M}) = 1$ in the spin-scalar-chiral state [19, 20], and $\chi = 0$ and $S(\mathrm{K}) = 1$ in the 120° Néel state.

Results.—We show the real-time dynamics in Fig. 2 when we apply a linearly polarized static electric field $\boldsymbol{F}(t) = -\dot{\boldsymbol{A}}(t) = (F_0, 0)$ with $F_0 = 0.5$, which precludes conventional mechanisms for inducing scalar chirality. See Supplemental Material [74] for the video of the spin configuration, spin scalar chirality, and structure factor. The dynamics can be divided into the following two stages. (i) The collapse of the FM order ($t \lesssim 100$): After the electric field is switched on at $t = 0$, the FM correlation $S(\Gamma) = S(0, 0)$ rapidly decays at $t \approx 40$ as shown in Fig. 2(b). At $t = 100$, the electrons uniformly occupy the lower band [the left panel of Fig. 2(c)], and $S(\boldsymbol{q})$ is finite near the Brillouin zone boundary [Fig. 2(f)]. The instability of the FM order is induced by the inverted electron distribution in the lower band due to the Bloch oscillation of the electrons [73, 74]. Here, the Bloch-oscillation period is given by $4\pi/F_0 \approx 25.1$, which is reflected in $S(\Gamma)$ shown in Fig. 2(b). (ii) The development of the spin scalar chirality ($t \gtrsim 100$): The scalar-chiral correlation $S(\mathrm{M})$ builds up linearly in time until $t \approx 3000$. The scalar chirality χ starts to increase at $t \approx 3000$, and then takes the maximal value ≈ 1.1 at $t = 5500$, as displayed in Fig. 2(a). The uniform spin-scalar-chiral structure is seen in Fig. 2(d). After $t \approx 5500$, the scalar chirality χ decreases down to ≈ -0.7 while $S(\mathrm{M})$ remains constant. In Fig. 2(e), we observe the spin-scalar-chiral state with $\chi < 0$ at $t = 8000$. For $t \gtrsim 3000$, the structure factor has three peaks at $\boldsymbol{q} = (\pi, -\pi/\sqrt{3})$, $(\pi, \pi/\sqrt{3})$, and $(0, 2\pi/\sqrt{3})$ as shown in

Figs. 2(g) and 2(h), although their values slightly deviate from 1/3. The sign of χ is unstable in time in the static field; we will later show that circularly polarized light can control and stabilize the sign.

Although the spin scalar chirality is not completely uniform as shown in Figs. 2(d) and 2(e), we can confirm the topological nature by calculating the Chern number $n_{\rm Ch}$. In aperiodic systems, such index is defined as [75–77][78]

$$n_{\rm Ch} \coloneqq \dim\ker[A-1] - \dim\ker[A+1], \tag{2}$$

where $A \coloneqq P_{\rm F} - \mathcal{D}_{\boldsymbol{a}}^{\dagger} P_{\rm F} \mathcal{D}_{\boldsymbol{a}}$, $P_{\rm F} = \sum_{\varepsilon_\nu \le \varepsilon_{\rm F}} |\nu\rangle\langle\nu|$, and $\mathcal{D}_{\boldsymbol{a}}(\boldsymbol{x}) \coloneqq \big[x+iy-(a_x+ia_y)\big]/\big|x+iy-(a_x+ia_y)\big|$. Here, $|\nu\rangle$ are eigenstates of the Hamiltonian (1), $\boldsymbol{x} = (x, y)$ is the position vector of the lattice points, and $\boldsymbol{a} = (a_x, a_y) \neq \boldsymbol{x}$ is a vector of a flux point (see, e.g., Refs. [79, 80] for detailed calculation). From Eq. (2), we obtain $n_{\rm Ch} = 1$ and -1 for the lowest band at $t = 5500$ [Fig. 2(d)] and $t = 8000$ [Fig. 2(e)], respectively, indicating that these spin-scalar-chiral states have a topological nature. However, the DC Hall conductivity would be canceled out in the photoinduced spin-scalar-chiral state since the total Chern number is zero for the effective half-filled case where the lower two bands are uniformly occupied, while we might see the Hall current or edge state during the decay process of itinerant electrons after switching off photoirradiation. Nevertheless, the photoinduced spin-scalar-chiral state can exhibit optical Hall effects owing to the nonzero Chern number because optical inter-band transitions are still allowed. The calculation of physical quantities for itinerant electrons reflecting the topological nature, such as optical Hall conductivity, in real-time evolution will be reported in a future article.

The appearance of the spin-scalar-chiral state is ascribed to that uniform electron distribution in the lower band which minimizes the total energy of the spin-scalar-chiral state rather than the FM state. As shown in Fig. 2(c), the electrons uniformly occupy the lower band(s) after the collapse of the FM order, implying that the energy bands are effectively half-filled. It was shown that the ground state of the present model at half filling is either 120° Néel or spin-scalar-chiral state depending on the NNN transfer integral h_2 [81], whereas we expect that the high-temperature state is paramagnetic, given the finite-temperature phase diagrams [24, 82]. Our results are roughly consistent with ground-state phase diagrams, suggesting that this spin-scalar-chiral state is not due to thermal excitations.

Next, we investigate the random tilt introduced into $\{\boldsymbol{S}_i\}$ at $t = 0$. Figures 3(a) and 3(b) show the time profiles of χ and $S(\mathrm{M})$ for 100 different initial configurations of $\{\boldsymbol{S}_i\}$. The scalar chirality appears for $t \gtrsim 2000$ and varies between -1.2 and 1.2, while the absolute value of the mean, plotted as the red curve, is always less than 0.2. This indicates that the sign of χ depends on the initial configurations and is not controlled by the static field; and thus, the present spin-scalar-chiral state is not due to the field-induced DM interactions. Meanwhile, $S(\mathrm{M})$, which reflects the long-range correlation of the scalar chirality, gradually builds up and is kept above 0.8 for

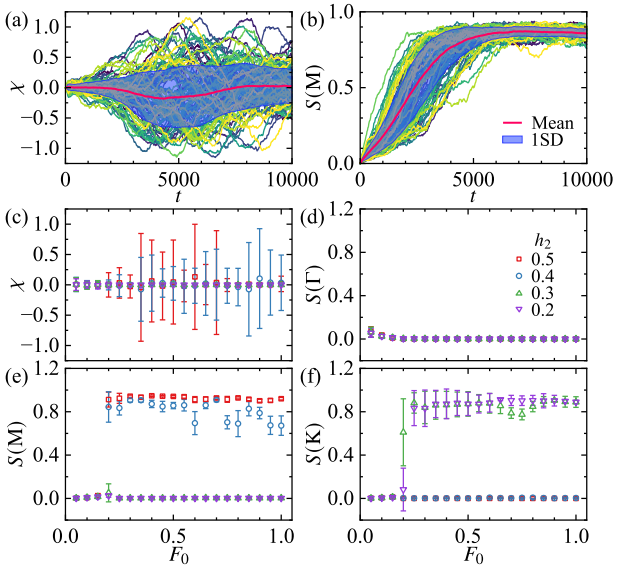


FIG. 3. Time profiles of (a) χ and (b) $S(\mathrm{M})$ with $h_2 = 0.4$. The red line and blue shade denote the mean and standard deviation at each time, respectively. (c)–(f) Mean and standard deviation at $t = 10000$ for $h_2 = 0.2$–0.5.

$t \gtrsim 5000$ even when $\chi \approx 0$. We also found that the short-range correlation of scalar chirality is stronger than that in disordered states [74]. Therefore, we consider the spin-scalar-chiral state to be stable in the thermodynamic limit, although the size of the domain with positive or negative chirality varies with time.

In Figs. 3(c)–3(f), we show the mean and standard deviation of the chirality and structure factor at $t = 10000$. The spin-scalar-chiral or 120° Néel state is stabilized for $F_0 \gtrsim 0.2$, depending on h_2. From these data, we sketch a "steady-state phase diagram" in Fig. 1(c), where there are three phases, i.e., the spin-scalar-chiral phase for $F_0 \gtrsim 0.2$ and $h_2 \gtrsim 0.4$, the 120° Néel phase for $F_0 \gtrsim 0.2$ and $h_2 \lesssim 0.3$, and the paramagnetic phase for $0 < F_0 \lesssim 0.2$.

The sign of the scalar chirality can be controlled by circular polarization. Figure 4(a) shows the time profiles of χ with left/right circularly polarized (LCP/RCP) light defined by $\boldsymbol{A}(t) = (F_0/\Omega)(\pm\cos\Omega t, \sin\Omega t)$ with $F_0 = 2.2$ and $\Omega = 1$, for 100 initial configurations. In the steady states, $\chi \approx 1.2$ for RCP and $\chi \approx -1.2$ for LCP light. The mean and standard deviation at $t = 10000$ are plotted in the inset of Fig. 4(a), as a function of F_0/Ω. The spin-scalar-chiral state is stabilized for $F_0/\Omega \gtrsim 1.4$, and the mean values of χ exhibit a non-monotonic behavior with respect to F_0/Ω, which is beyond the perturbation theory for the coupling between scalar chirality and circular polarization [54]. Furthermore, the signs of χ for LCP and RCP light are opposite to each other, while the mean values of χ for linearly polarized (LP) light $\boldsymbol{A}(t) = (F_0/\Omega)(\sin\Omega t, 0)$ are almost zero. Note that the controllability of the sign of χ is observed for $\Omega = 1$ but not for $\Omega = 20$ and 40 (not shown); this may imply that the light frequency should be comparable to the transfer integral h_1 and much smaller than the band gap ($\sim 2J$). A detailed analysis for the circular polarization is left

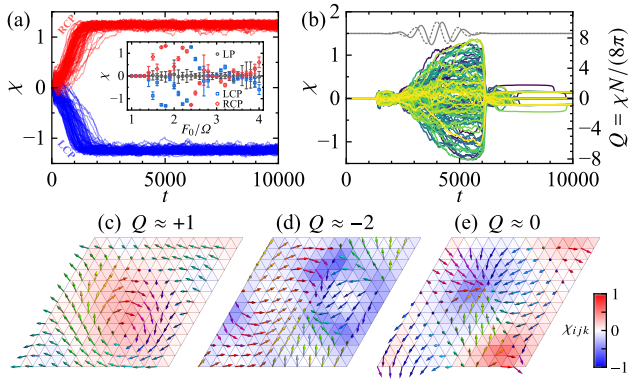


FIG. 4. (a) Time profiles of χ with the RCP (red lines) and LCP (blue lines) light with $F_0 = 2.2$ and $\Omega = 1$. The inset shows the mean and standard deviation at $t = 10000$ as a function of F_0/Ω. (b) Time profiles of χ with an RCP pulse. The electric field of the x (y) component is plotted as the gray solid (dashed) line. Parameters are set to $F_0 = 1.8$, $\Omega = 2\pi/1000$, and $\delta\theta_{\max} = 1$. (c)–(e) Snapshots of the spin structure and local scalar chirality at $t = 8000$. NNN transfer integral is set to $h_2 = 0.5$ in (a)–(e).

for future work.

Lastly, we demonstrate the real-time dynamics induced by an RCP pulse that contains a few optical cycles, $\boldsymbol{A}(t) = (F_0/\Omega)\exp[-(t-t_0)^2/(2t_w^2)](\cos[\Omega(t-t_0)], -\sin[\Omega(t-t_0)])$ with $t_0 = 4000$ and $t_w = 800$. In Fig. 4(b), we observe that the scalar chirality develops up to ± 1.2 during irradiation and rapidly decays after irradiation. However, the sign of χ is not controlled by either RCP or LCP pulse since the central frequency of the pulse, $\Omega = 2\pi/1000 \approx 0.0063 \ll h_1$, is quite low, so that the dynamics are close to those in the static field. Here, the advantage of the circularly polarized pulse is that the magnitude of the electric field does not vanish during irradiation in contrast to the LP pulse, which prevents the relaxation to the FM ground state and promotes the growth of χ.

After pulse irradiation, a metastable state with approximate integer $Q = \chi N/(2 \times 4\pi)$ is realized, and it survives until $t \sim 10000$. Here, Q is the Pontryagin number [74, 83], which counts the net number of skyrmions in the cluster. At $t = 8000$, a skyrmion-like magnetic object is observed in Figs. 4(c)–4(e). When a single skyrmion is present as shown in Fig. 4(c), Q is approximately equal to ± 1. In the present calculations for $N = 12 \times 12$, we also observe states with $|Q| \approx 2$ as displayed in Fig. 4(d). Figure 4(e) exemplifies a state in which both $Q \approx 1$ and $Q \approx -1$ objects are created while the total Q is cancelled out. The lifetime of the metastable states depends on the relaxation rate, i.e., the Gilbert damping constant α in the present calculations; we found that the lifetime increases with decreasing α as expected. Note that the metastable skyrmions can be excited by the LP pulse as well and even without h_2.

Discussion.—The required magnitude of the electric field is estimated to be of the order of $\hbar/(ea\tau) \sim 1$ MV/cm with τ being an intraband relaxation time [73] (typically, $\tau \gtrsim 10$ fs). This magnitude is so strong that materials will be damaged by the static field. However, this problem can be circumvented by using a short terahertz pulse [84], as demonstrated in Fig. 4.

The time scale of the dynamics is determined by the Gilbert damping constant α as well as the field magnitude. In real materials in equilibrium, α is of order 0.001–0.01 [85], which is two or three orders of magnitude smaller than $\alpha = 1$ adopted here. We found that, for $\alpha = 0.01$, the long-range spin-scalar-chiral or 120° Néel order is suppressed in the steady states. If a large α of order 1 is essential, the realization of these photoinduced orders would be difficult. Theoretically, we might overcome this difficulty by introducing another magnetic interaction that favors the spin-scalar-chiral state, e.g., antiferromagnetic (AFM) interaction between the localized spins [20, 86, 87], or by considering the dissipation due to electron-electron interactions far from equilibrium.

Summary and outlook.—We have investigated the real-time dynamics in a centrosymmetric itinerant magnet and found that the spin-scalar-chiral or 120° Néel state is stabilized by the static field, continuous-wave light, and low-frequency pulse, depending on the NNN transfer integral. The sign of scalar chirality can be selected by circular polarization. Additionally, skyrmions are created in metastable states after pulse irradiation, characterized by the Pontryagin number. These spin-scalar-chiral states and metastable skyrmion states arise from the non-thermal electron distribution, not from antisymmetric interactions such as the DM interaction. The underlying mechanism should be further clarified in future work.

Recently, it was revealed that the AFM skyrmion-like textures are transiently created on the centrosymmetric square lattice [88]. In this study, however, the spin-scalar-chiral state is stable under optical fields and controllable by circular polarization. Furthermore, contrary to the conventional theory [54], our results demonstrate that neither the DM interaction nor circular polarization is necessary for the spin-scalar-chiral state; the absence of antisymmetric interactions makes the optical switching of scalar chirality easier. These findings suggest that centrosymmetric magnets are promising for ultrafast control of scalar chirality.

This work was supported by JSPS KAKENHI Grant Nos. JP18H05208, JP19K23419, JP20K14394, JP23K13052, JP23H01108, JP20K14411, and JSPS Grant-in-Aid for Scientific Research on Innovative Areas "Quantum Liquid Crystals" (KAKENHI Grant Nos. JP20H05154 and JP22H04469). Y.A. is supported by JST PRESTO Grant No. JPMJPR2251. The early stage of this work started from the 9th workshop on "Frontier of Theory for Condensed Matter Systems" in Hokkaido in 2020. The numerical calculations were performed using the facilities of the Supercomputer Center, the Institute for Solid State Physics, the University of Tokyo.

[1] S. Seki and M. Mochizuki, *Skyrmions in Magnetic Materials* (Springer, Cham, 2016).
[2] J. H. Han, *Skyrmions in Condensed Matter* (Springer, Cham, 2017).

[3] J. Zang, V. Cros, and A. Hoffmann, eds., *Topology in Magnetism* (Springer, Cham, 2017).

[4] T. Blachowicz and A. Ehrmann, *Spintronics: Theory, Modelling, Devices* (De Gruyter, Berlin, 2019).

[5] N. Nagaosa and Y. Tokura, Topological properties and dynamics of magnetic skyrmions, Nat. Nanotechnol. **8**, 899 (2013).

[6] H. Ochoa and Y. Tserkovnyak, Quantum skyrmionics, Int. J. Mod. Phys. B **33**, 1930005 (2019).

[7] C. Back, V. Cros, H. Ebert, K. Everschor-Sitte, A. Fert, M. Garst, T. Ma, S. Mankovsky, T. L. Monchesky, M. Mostovoy, N. Nagaosa, S. S. P. Parkin, C. Pfleiderer, N. Reyren, A. Rosch, Y. Taguchi, Y. Tokura, K. von Bergmann, and J. Zang, The 2020 skyrmionics roadmap, J. Phys. D. Appl. Phys. **53**, 363001 (2020).

[8] Y. Fujishiro, N. Kanazawa, and Y. Tokura, Engineering skyrmions and emergent monopoles in topological spin crystals, Appl. Phys. Lett. **116**, 090501 (2020).

[9] Y. Tokura and N. Kanazawa, Magnetic Skyrmion Materials, Chem. Rev. **121**, 2857 (2021).

[10] C. D. Batista, S.-Z. Lin, S. Hayami, and Y. Kamiya, Frustration and chiral orderings in correlated electron systems, Rep. Prog. Phys. **79**, 084504 (2016).

[11] S. Hayami and Y. Motome, Topological spin crystals by itinerant frustration, J. Phys. Condens. Matter **33**, 443001 (2021).

[12] T. Kurumaji, T. Nakajima, M. Hirschberger, A. Kikkawa, Y. Yamasaki, H. Sagayama, H. Nakao, Y. Taguchi, T.-h. Arima, and Y. Tokura, Skyrmion lattice with a giant topological Hall effect in a frustrated triangular-lattice magnet, Science **365**, 914 (2019).

[13] M. Hirschberger, T. Nakajima, S. Gao, L. Peng, A. Kikkawa, T. Kurumaji, M. Kriener, Y. Yamasaki, H. Sagayama, H. Nakao, K. Ohishi, K. Kakurai, Y. Taguchi, X. Yu, T.-h. Arima, and Y. Tokura, Skyrmion phase and competing magnetic orders on a breathing kagomé lattice, Nat. Commun. **10**, 5831 (2019).

[14] N. D. Khanh, T. Nakajima, X. Yu, S. Gao, K. Shibata, M. Hirschberger, Y. Yamasaki, H. Sagayama, H. Nakao, L. Peng, K. Nakajima, R. Takagi, T.-h. Arima, Y. Tokura, and S. Seki, Nanometric square skyrmion lattice in a centrosymmetric tetragonal magnet, Nat. Nanotechnol. **15**, 444 (2020).

[15] Y. Yasui, C. J. Butler, N. D. Khanh, S. Hayami, T. Nomoto, T. Hanaguri, Y. Motome, R. Arita, T.-h. Arima, Y. Tokura, and S. Seki, Imaging the coupling between itinerant electrons and localised moments in the centrosymmetric skyrmion magnet $GdRu_2Si_2$, Nat. Commun. **11**, 5925 (2020).

[16] T. Okubo, S. Chung, and H. Kawamura, Multiple-q States and the Skyrmion Lattice of the Triangular-Lattice Heisenberg Antiferromagnet under Magnetic Fields, Phys. Rev. Lett. **108**, 017206 (2012).

[17] A. O. Leonov and M. Mostovoy, Multiply periodic states and isolated skyrmions in an anisotropic frustrated magnet, Nat. Commun. **6**, 8275 (2015).

[18] D. Amoroso, P. Barone, and S. Picozzi, Spontaneous skyrmionic lattice from anisotropic symmetric exchange in a Ni-halide monolayer, Nat. Commun. **11**, 5784 (2020).

[19] I. Martin and C. D. Batista, Itinerant Electron-Driven Chiral Magnetic Ordering and Spontaneous Quantum Hall Effect in Triangular Lattice Models, Phys. Rev. Lett. **101**, 156402 (2008).

[20] Y. Akagi and Y. Motome, Spin Chirality Ordering and Anomalous Hall Effect in the Ferromagnetic Kondo Lattice Model on a Triangular Lattice, J. Phys. Soc. Jpn. **79**, 083711 (2010).

[21] Y. Akagi, M. Udagawa, and Y. Motome, Hidden Multiple-Spin Interactions as an Origin of Spin Scalar Chiral Order in Frustrated Kondo Lattice Models, Phys. Rev. Lett. **108**, 096401 (2012).

[22] R. Ozawa, S. Hayami, and Y. Motome, Zero-Field Skyrmions with a High Topological Number in Itinerant Magnets, Phys. Rev. Lett. **118**, 147205 (2017).

[23] S. Hayami, R. Ozawa, and Y. Motome, Effective bilinear-biquadratic model for noncoplanar ordering in itinerant magnets, Phys. Rev. B **95**, 224424 (2017).

[24] S. Kumar and J. van den Brink, Frustration-Induced Insulating Chiral Spin State in Itinerant Triangular-Lattice Magnets, Phys. Rev. Lett. **105**, 216405 (2010).

[25] M. Lee, W. Kang, Y. Onose, Y. Tokura, and N. P. Ong, Unusual Hall Effect Anomaly in MnSi under Pressure, Phys. Rev. Lett. **102**, 186601 (2009).

[26] A. Neubauer, C. Pfleiderer, B. Binz, A. Rosch, R. Ritz, P. G. Niklowitz, and P. Böni, Topological Hall Effect in the A Phase of MnSi, Phys. Rev. Lett. **102**, 186602 (2009).

[27] Y. Shiomi, N. Kanazawa, K. Shibata, Y. Onose, and Y. Tokura, Topological Nernst effect in a three-dimensional skyrmion-lattice phase, Phys. Rev. B **88**, 064409 (2013).

[28] M. Hirschberger, L. Spitz, T. Nomoto, T. Kurumaji, S. Gao, J. Masell, T. Nakajima, A. Kikkawa, Y. Yamasaki, H. Sagayama, H. Nakao, Y. Taguchi, R. Arita, T.-h. Arima, and Y. Tokura, Topological Nernst Effect of the Two-Dimensional Skyrmion Lattice, Phys. Rev. Lett. **125**, 076602 (2020).

[29] S. K. Kim, K. Nakata, D. Loss, and Y. Tserkovnyak, Tunable Magnonic Thermal Hall Effect in Skyrmion Crystal Phases of Ferrimagnets, Phys. Rev. Lett. **122**, 057204 (2019).

[30] H. Ishizuka and N. Nagaosa, Anomalous electrical magnetochiral effect by chiral spin-cluster scattering, Nat. Commun. **11**, 2986 (2020).

[31] Y. Fujishiro, N. Kanazawa, R. Kurihara, H. Ishizuka, T. Hori, F. S. Yasin, X. Yu, A. Tsukazaki, M. Ichikawa, M. Kawasaki, N. Nagaosa, M. Tokunaga, and Y. Tokura, Giant anomalous Hall effect from spin-chirality scattering in a chiral magnet, Nat. Commun. **12**, 317 (2021).

[32] Y. Hayashi, Y. Okamura, N. Kanazawa, T. Yu, T. Koretsune, R. Arita, A. Tsukazaki, M. Ichikawa, M. Kawasaki, Y. Tokura, and Y. Takahashi, Magneto-optical spectroscopy on Weyl nodes for anomalous and topological Hall effects in chiral MnGe, Nat. Commun. **12**, 5974 (2021).

[33] S. Sorn, L. Yang, and A. Paramekanti, Resonant optical topological Hall conductivity from skyrmions, Phys. Rev. B **104**, 134419 (2021).

[34] W. Feng, J.-p. Hanke, X. Zhou, G.-y. Guo, S. Blügel, Y. Mokrousov, and Y. Yao, Topological magneto-optical effects and their quantization in noncoplanar antiferromagnets, Nat. Commun. **11**, 118 (2020).

[35] S. Okumura, T. Morimoto, Y. Kato, and Y. Motome, Quadratic optical responses in a chiral magnet, Phys. Rev. B **104**, L180407 (2021).

[36] M. Mochizuki, N. Furukawa, and N. Nagaosa, Theory of Electromagnons in the Multiferroic Mn Perovskites: The Vital Role of Higher Harmonic Components of the Spiral Spin Order, Phys. Rev. Lett. **104**, 177206 (2010).

[37] M. Mochizuki and N. Nagaosa, Theoretically Predicted Picosecond Optical Switching of Spin Chirality in Multiferroics, Phys. Rev. Lett. **105**, 147202 (2010).

[38] T. Kubacka, J. A. Johnson, M. C. Hoffmann, C. Vicario, S. de Jong, P. Beaud, S. Grubel, S.-W. Huang, L. Huber, L. Patthey, Y.-D. Chuang, J. J. Turner, G. L. Dakovski, W.-S. Lee, M. P. Minitti, W. Schlotter, R. G. Moore, C. P. Hauri, S. M. Koohpayeh, V. Scagnoli, G. Ingold, S. L. Johnson, and U. Staub, Large-Amplitude Spin Dynamics Driven by a THz Pulse in Resonance with an Electromagnon, Science **343**, 1333 (2014).

[39] Y. Yamasaki, H. Nakao, Y. Murakami, T. Nakajima, A. L. Sampietro, H. Ohsumi, M. Takata, T. Arima, and Y. Tokura, X-ray induced lock-in transition of cycloidal magnetic order in a multiferroic perovskite manganite, Phys. Rev. B **91**, 100403(R) (2015).

[40] M. Sato, S. Takayoshi, and T. Oka, Laser-Driven Multiferroics and Ultrafast Spin Current Generation, Phys. Rev. Lett. **117**, 147202 (2016).

[41] P. Khan, M. Kanamaru, K. Matsumoto, T. Ito, and T. Satoh, Ultrafast light-driven simultaneous excitation of coherent terahertz magnons and phonons in multiferroic $BiFeO_3$, Phys. Rev. B **101**, 134413 (2020).

[42] M. Finazzi, M. Savoini, A. R. Khorsand, A. Tsukamoto, A. Itoh, L. Duò, A. Kirilyuk, T. Rasing, and M. Ezawa, Laser-Induced Magnetic Nanostructures with Tunable Topological Properties, Phys. Rev. Lett. **110**, 177205 (2013).

[43] W. Koshibae and N. Nagaosa, Creation of skyrmions and antiskyrmions by local heating, Nat. Commun. **5**, 5148 (2014).

[44] N. Ogawa, S. Seki, and Y. Tokura, Ultrafast optical excitation of magnetic skyrmions, Sci. Rep. **5**, 9552 (2015).

[45] C. Heo, N. S. Kiselev, A. K. Nandy, S. Blügel, and T. Rasing, Switching of chiral magnetic skyrmions by picosecond magnetic field pulses via transient topological states, Sci. Rep. **6**, 27146 (2016).

[46] V. Flovik, A. Qaiumzadeh, A. K. Nandy, C. Heo, and T. Rasing, Generation of single skyrmions by picosecond magnetic field pulses, Phys. Rev. B **96**, 140411(R) (2017).

[47] G. Berruto, I. Madan, Y. Murooka, G. M. Vanacore, E. Pomarico, J. Rajeswari, R. Lamb, P. Huang, A. J. Kruchkov, Y. Togawa, T. LaGrange, D. McGrouther, H. M. Rønnow, and F. Carbone, Laser-Induced Skyrmion Writing and Erasing in an Ultrafast Cryo-Lorentz Transmission Electron Microscope, Phys. Rev. Lett. **120**, 117201 (2018).

[48] H. Fujita and M. Sato, Ultrafast generation of skyrmionic defects with vortex beams: Printing laser profiles on magnets, Phys. Rev. B **95**, 054421 (2017).

[49] S.-G. Je, P. Vallobra, T. Srivastava, J.-C. Rojas-Sánchez, T. H. Pham, M. Hehn, G. Malinowski, C. Baraduc, S. Auffret, G. Gaudin, S. Mangin, H. Béa, and O. Boulle, Creation of Magnetic Skyrmion Bubble Lattices by Ultrafast Laser in Ultrathin Films, Nano Lett. **18**, 7362 (2018).

[50] W. Yang, H. Yang, Y. Cao, and P. Yan, Photonic orbital angular momentum transfer and magnetic skyrmion rotation, Opt. Express **26**, 8778 (2018).

[51] A. de la Torre, D. M. Kennes, M. Claassen, S. Gerber, J. W. McIver, and M. A. Sentef, Colloquium: Nonthermal pathways to ultrafast control in quantum materials, Rev. Mod. Phys. **93**, 041002 (2021).

[52] M. Bukov, M. Kolodrubetz, and A. Polkovnikov, Schrieffer-Wolff Transformation for Periodically Driven Systems: Strongly Correlated Systems with Artificial Gauge Fields, Phys. Rev. Lett. **116**, 125301 (2016).

[53] J. M. Losada, A. Brataas, and A. Qaiumzadeh, Ultrafast control of spin interactions in honeycomb antiferromagnetic insulators, Phys. Rev. B **100**, 060410(R) (2019).

[54] K. Taguchi, J.-i. Ohe, and G. Tatara, Ultrafast Magnetic Vortex Core Switching Driven by the Topological Inverse Faraday Effect, Phys. Rev. Lett. **109**, 127204 (2012).

[55] M. Claassen, H.-C. Jiang, B. Moritz, and T. P. Devereaux, Dynamical time-reversal symmetry breaking and photo-induced chiral spin liquids in frustrated Mott insulators, Nat. Commun. **8**, 1192 (2017).

[56] S. Kitamura, T. Oka, and H. Aoki, Probing and controlling spin chirality in Mott insulators by circularly polarized laser, Phys. Rev. B **96**, 014406 (2017).

[57] R. Eto and M. Mochizuki, Dynamical switching of magnetic topology in microwave-driven itinerant magnet, Phys. Rev. B **104**, 104425 (2021).

[58] S. A. Owerre, Floquet topological magnons, J. Phys. Commun. **1**, 021002 (2017).

[59] E. V. Boström, M. Claassen, J. McIver, G. Jotzu, A. Rubio, and M. Sentef, Light-induced topological magnons in two-dimensional van der Waals magnets, SciPost Phys. **9**, 061 (2020).

[60] E. A. Stepanov, C. Dutreix, and M. I. Katsnelson, Dynamical and Reversible Control of Topological Spin Textures, Phys. Rev. Lett. **118**, 157201 (2017).

[61] E. V. Boström, A. Rubio, and C. Verdozzi, Microscopic theory of light-induced ultrafast skyrmion excitation in transition metal films, npj Comput. Mater. **8**, 62 (2022).

[62] V. L. Quito and R. Flint, Floquet Engineering Correlated Materials with Unpolarized Light, Phys. Rev. Lett. **126**, 177201 (2021).

[63] H. Kobayashi, R. Fujiuchi, K. Sugimoto, and Y. Ohta, Light-induced switching of magnetic order in the anisotropic triangular-lattice Hubbard model, Phys. Rev. B **103**, L161106 (2021).

[64] T. Inoue and M. Mochizuki, Photoinduced 120-degree spin order in the Kondo-lattice model on a triangular lattice, Phys. Rev. B **105**, 144422 (2022).

[65] S. Ghosh, F. Freimuth, O. Gomonay, S. Blügel, and Y. Mokrousov, Driving spin chirality by electron dynamics in laser-excited antiferromagnets, Commun. Phys. **5**, 69 (2022).

[66] D. Yudin, D. R. Gulevich, and M. Titov, Light-Induced Anisotropic Skyrmion and Stripe Phases in a Rashba Ferromagnet, Phys. Rev. Lett. **119**, 147202 (2017).

[67] S. Ø. Hanslin and A. Qaiumzadeh, Light-induced Dzyaloshinskii-Moriya interactions in antiferromagnetic metals, Phys. Rev. B **103**, 134428 (2021).

[68] S. C. Furuya and M. Sato, Electric-Field Control of Magnetic Anisotropies: Applications to Kitaev Spin Liquids and Topological Spin Textures, arXiv:2110.06503.

[69] W. Koshibae, N. Furukawa, and N. Nagaosa, Real-Time Quantum Dynamics of Interacting Electrons: Self-Organized Nanoscale Structure in a Spin-Electron Coupled System, Phys. Rev. Lett. **103**, 266402 (2009).

[70] G.-W. Chern, K. Barros, Z. Wang, H. Suwa, and C. D. Batista, Semiclassical dynamics of spin density waves, Phys. Rev. B **97**, 035120 (2018).

[71] A. Ono and S. Ishihara, Double-Exchange Interaction in Optically Induced Nonequilibrium State: A Conversion from Ferromagnetic to Antiferromagnetic Structure, Phys. Rev. Lett. **119**, 207202 (2017).

[72] A. Ono and S. Ishihara, Photocontrol of magnetic structure in an itinerant magnet, Phys. Rev. B **98**, 214408 (2018).

[73] A. Ono and S. Ishihara, Electric-Field-Induced Antiferromagnetic Insulating State in a Metallic Ferromagnet, J. Phys. Soc. Jpn. **89**, 095001 (2020).

[74] See Supplemental Material at https URL.

[75] J. E. Avron, R. Seiler, and B. Simon, Charge deficiency, charge transport and comparison of dimensions, Commun. Math. Phys. **159**, 399 (1994).

[76] J. E. Avron, R. Seiler, and B. Simon, The Index of a Pair of Projections, J. Funct. Anal. **120**, 220 (1994).

[77] M. Aizenman and G. M. Graf, Localization bounds for an electron gas, J. Phys. A **31**, 6783 (1998).

[78] We have other expressions of the Chern number in aperiodic systems, such as the Bott index (see, e.g., Refs. [89–91]) and the Chern number in the real space [92, 93]. The nonzero index

corresponds to the system showing the topological Hall effect.
[79] Y. Akagi, H. Katsura, and T. Koma, A New Numerical Method for $\mathbb{Z}_2$ Topological Insulators with Strong Disorder, J. Phys. Soc. Jpn. **86**, 123710 (2017).
[80] Y. Akagi, Topological Invariant for Bosonic Bogoliubov–de Gennes Systems with Disorder, J. Phys. Soc. Jpn. **89**, 123601 (2020).
[81] The details will be reported elsewhere.
[82] D. S. Kathyat, A. Mukherjee, and S. Kumar, Microscopic magnetic Hamiltonian for exotic spin textures in metals, Phys. Rev. B **102**, 075106 (2020).
[83] V. Lohani, C. Hickey, J. Masell, and A. Rosch, Quantum Skyrmions in Frustrated Ferromagnets, Phys. Rev. X **9**, 041063 (2019).
[84] J. A. Fülöp, S. Tzortzakis, and T. Kampfrath, Laser-Driven Strong-Field Terahertz Sources, Adv. Opt. Mater. **8**, 1900681 (2020).
[85] S. Maekawa, S. O. Valenzuela, E. Saitoh, and T. Kimura, eds., *Spin Current*, 2nd ed. (Oxford University Press, Oxford, 2017).
[86] Y. Akagi and Y. Motome, Noncoplanar spin canting in lightly-doped ferromagnetic Kondo lattice model on a triangular lattice, J. Phys. Conf. Ser. **320**, 012059 (2011).
[87] Y. Akagi and Y. Motome, Spontaneous formation of kagome network and Dirac half-semimetal on a triangular lattice, Phys. Rev. B **91**, 155132 (2015).
[88] A. Ono and S. Ishihara, Photoinduced Topological Spin Texture in a Metallic Ferromagnet, J. Phys. Soc. Jpn. **88**, 023703 (2019).
[89] J. Bellissard, A. van Elst, and H. Schulz-Baldes, The noncommutative geometry of the quantum Hall effect, J. Math. Phys. **35**, 5373 (1994).
[90] M. B. Hastings and T. A. Loring, Almost commuting matrices, localized Wannier functions, and the quantum Hall effect, J. Math. Phys. **51**, 015214 (2010).
[91] T. A. Loring and M. B. Hastings, Disordered topological insulators via C^*-algebras, Europhys. Lett. **92**, 67004 (2010).
[92] A. Kitaev, Anyons in an exactly solved model and beyond, Ann. Phys. **321**, 2 (2006).
[93] E. Prodan, T. L. Hughes, and B. A. Bernevig, Entanglement spectrum of a disordered topological chern insulator, Phys. Rev. Lett. **105**, 115501 (2010).